Synthesized Light Transients

A. Wirth,[1] M. Th. Hassan,[1,2] I. Grguraš,[1] J. Gagnon,[1] A. Moulet,[1] T. T. Luu,[1]
S. Pabst,[3,4] R. Santra,[3,4] Z. A. Alahmed,[2] A. M. Azzeer,[2] V. S. Yakovlev,[1,5]
V. Pervak,[5] F. Krausz,[1,5] E. Goulielmakis[1]*

Manipulation of electron dynamics calls for electromagnetic forces that can be confined to and controlled over sub-femtosecond time intervals. Tailored transients of light fields can provide these forces. We report on the generation of subcycle field transients spanning the infrared, visible, and ultraviolet frequency regimes with a 1.5-octave three-channel optical field synthesizer and their attosecond sampling. To demonstrate applicability, we field-ionized krypton atoms within a single wave crest and launched a valence-shell electron wavepacket with a well-defined initial phase. Half-cycle field excitation and attosecond probing revealed fine details of atomic-scale electron motion, such as the instantaneous rate of tunneling, the initial charge distribution of a valence-shell wavepacket, the attosecond dynamic shift (instantaneous ac Stark shift) of its energy levels, and its few-femtosecond coherent oscillations.

The generation and measurement (briefly, synthesis) of electric field transients permitted the characterization of electric circuits with sub-picosecond temporal resolution (*1*) and constitutes a base technology for advancing high-speed electronics and electron-based information technologies. Electronic processes on the atomic scale typically evolve on a few-femtosecond to sub-femtosecond time scale. Time-domain access to these dynamics requires the extension of electric field control to optical frequencies.

As a first step to this end, measurement (*2, 3*) and control (*4–9*) of the phase of field oscillations relative to their envelope [carrier-envelope phase (CEP)] yielded reproducible few-cycle light waveforms (*10*). Attosecond metrology (*11*) was further advanced by the reproducible generation and measurement of isolated attosecond pulses

[1]Max-Planck-Institut für Quantenoptik (MPQ), Hans-Kopfermann-Strasse 1, D-85748 Garching, Germany. [2]Department of Physics and Astronomy, King Saud University, Riyadh 11451, Kingdom of Saudi Arabia. [3]Center for Free-Electron Laser Science, Deutsches Elektronen Synchrotron, Notkestrasse 85, 22607 Hamburg, Germany. [4]Department of Physics, University of Hamburg, Jungiusstrasse 9, 20355 Hamburg, Germany. [5]Department für Physik, Ludwig-Maximilians-Universität (LMU), Am Coulombwall 1, D-85748 Garching, Germany.

*To whom correspondence should be addressed. E-mail: elgo@mpq.mpg.de

Fig. 1. Apparatus for infrared-visible-ultraviolet field synthesis. (**A**) Schematic representation of a prototypical three-channel light field synthesizer. (**B**) Spectrum of the coherent radiation at the exit of the hollow-core fiber (dashed line). Spectra exiting the individual channels (not to scale) are shown in red for Ch_{NIR} (700 to 1100 nm), yellow for Ch_{VIS} (500 to 700 nm), and blue for Ch_{VIS-UV} (350 to 500 nm). (**C**) Temporal intensity (solid lines) and phase profiles (dashed curves) of the respective pulses. The thin black lines depict the intensity profiles of the corresponding bandwidth-limited pulses, with durations of $\tau_{Ch(NIR)} = 6.8$ fs, $\tau_{Ch(VIS)} = 5$ fs, and $\tau_{Ch(VIS-UV)} = 4.5$ fs. Insets show photos of the respective beam profiles taken at the exit of the apparatus.
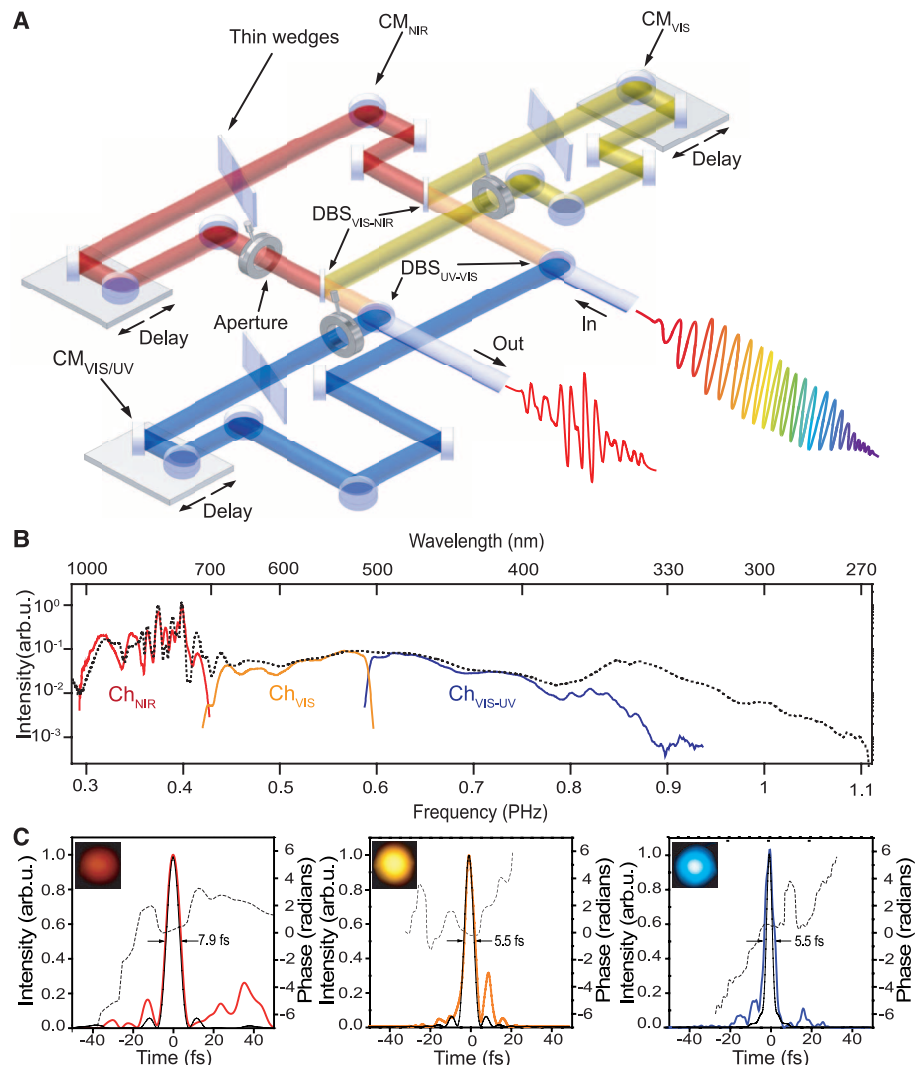
(12–14). Control (15) and real-time observation (16–21) of electronic processes would greatly benefit from sub-femtosecond sculpting and confinement of strong light fields. We are able to demonstrate this capability along with some of its consequences.

Tailoring light fields on the electronic time scale requires the coherent superposition and manipulation of frequencies over more than an octave in the visible and flanking spectral ranges. So far, this demand could only be met through the technique of molecular modulation (22–27). This approach recently allowed the subcycle shaping of optical fields via the superposition of quasi-monochromatic waves in the infrared-visible range (28). Although these periodic waveforms are highly relevant to advancing modern electronics, time-domain access to electronic phenomena calls for the temporal confinement of the sculpted waveform to a single cycle or just a few oscillation cycles. We refer to such super-octave optical waveforms as light transients. Recent experiments have paved the way toward the synthesis of light transients (29–33), but they have not yet achieved the goal of subcycle field shaping and measurement.

Here, we report on the shaping, confinement, and attosecond sampling of the fields of intense light transients within their carrier wave cycle (~2.4 fs) over the frequency band of 0.3 to 0.9 PHz. A variety of on-demand waveforms with controlled subcycle field evolution, yielding sub-femtosecond rise times or subcycle confinement of instantaneous intensity, demonstrate the power of PHz field synthesis. As an application of enhanced atomic-scale electron con-

trol, we field-ionized atoms within a single wave crest and triggered valence electron motion on a sub-femtosecond scale. By providing a sub-femtosecond optical field trigger and a robust attosecond probe, subcycle light transients establish sub-femtosecond pump-probe spectroscopy.

1.5-octave optical field synthesizer. We produced coherent supercontinua by propagating ~0.8 mJ, ~25-fs pulses carried at a wavelength of $\lambda_0 \sim 780$ nm in a hollow-core fiber filled with neon gas. Spectral broadening was enhanced with respect to previous experiments (34) by raising the gas pressure to ~3.5 bar, resulting in a nearly uniform (to within 20 dB) energy distribution over a bandwidth of >0.6 PHz (330 to 1100 nm) (Fig. 1B). Manipulation of individual spectral components requires their spatial separation and subsequent recombination. The conventional approach, based on prisms and liquid crystal modulators (31), is hardly scalable for super-octave–spanning operation; therefore, we instead implemented chirped multilayer mirror technology, proposed in (34), which offers scalability to several octaves in the visible and nearby spectral regions. Our prototypical three-channel device (Fig. 1A) subdivides the aforementioned ~0.6-PHz spectral range into three bands of nearly equal width—Ch_{NIR}, 700 to 1100 nm; Ch_{VIS}, 500 to 700 nm; and Ch_{VIS-UV}, 350 to 500 nm—with the help of dichroic beamsplitters $DBS_{VIS-NIR}$ and DBS_{UV-VIS} (fig. S1). Dispersive chirped mirrors $CM_{VIS/UV}$, CM_{VIS}, and CM_{NIR} compensate for the chirp carried by the pulse as well as that introduced by the thin fused silica wedge pairs incorporated in each channel and the beamsplitters

near the edges of the spectral bands. As a result, the pulses in the individual channels are compressed close to their bandwidth-limited durations (Fig. 1C).

The chirp, the CEP, and the delay of the pulses formed in Ch_{NIR}, Ch_{VIS}, and Ch_{VIS-UV} can be precisely controlled by wedges and nanometer-precision delay stages, respectively. The adjustment of the beam size in each channel—via an iris—allows control of the pulse's energy [supporting online material (SOM) text, section 1]. These control knobs offer both subcycle shaping of the generated fields and compression close to their bandwidth limit. Owing to the high efficiency of the chirped multilayer optics used (fig. S2), the device transmits some ~83% of the incident continuum beam (Fig. 1B, dotted line), resulting in a pulse energy of ~0.3 mJ/pulse at the exit of the apparatus ($Ch_{NIR} \sim 250$ μJ, $Ch_{VIS} \sim 35$ μJ, and $Ch_{VIS-UV} \sim 15$ μJ). The setup is assembled on a monolithic aluminum base plate, with active thermal and interferometric path-length stabilization (fig. S3).

By analogy with femtosecond electro-optic sampling of THz transients (1), we can use attosecond streaking (12, 35) for sampling the electric field of PHz transients. To this end, the PHz transients exiting our three-channel synthesizer were gently focused (to a peak intensity of ~10^{14} W/cm^2) into a neon gas jet, where they generated broadband extreme ultraviolet (XUV) radiation (14) emitted in a near-diffraction-limited beam collinear with the driving radiation (SOM text, section 2). Bandpass filtering (width of ~13 eV centered at ~85 eV) near the cut-off energy (~90 eV), implemented with multilayer

Fig. 2. Synthesis of petahertz light field transients. (**A** to **F**) Attosecond streaking spectrograms composed of photoelectron spectra normalized to their integral (left) and the respective retrieved electric fields (middle) and instantaneous intensity (right). Relative intensities for the most intense field crests—normalized to the maximum—are given in brackets. From (A) to (C), the delay of Ch_{VIS-UV} is varied in steps of 200 as (~π/4). Dashed black lines in (B) and (C) show the field transients calculated from the reference waveform of (A). (D) Relative delays and CEPs of the individual channels are adjusted so as to create twin transients with a field minimum in between them. (E) Ch_{NIR} is delayed by 1.45 fs (~π), resulting in a high-frequency leading transient followed by a low-frequency tail. The dashed line in (E) shows the field transients calculated from the reference waveform of (D). Transients in (A) to (C), (E), and (F) carry less than one cycle within the FWHM of their temporal intensity profile. (F) $\tau_{FWHM} \sim 2.1$ fs, incorporating only ~0.88 field cycles at the carrier wavelength of $\lambda_0 \sim 710$ nm.
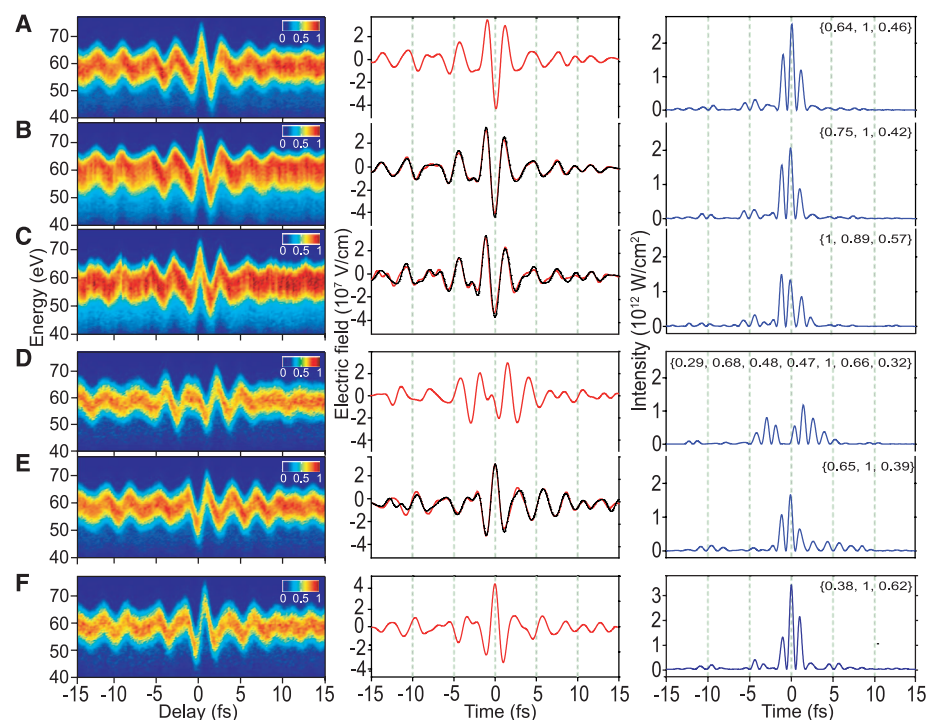
optics and thin metal foils, isolated a single attosecond pulse (12, 14). Both pulses were then focused into a second neon gas jet placed near the entrance of a time-of-flight electron spectrometer (TOF) for measuring the XUV-induced, laser-field–streaked photoelectron spectra versus delay (an attosecond streaking spectrogram) (35).

Attosecond streaking spectrograms of subcycle waveforms synthesized from near-bandwidth–limited fields exiting Ch_{NIR}, Ch_{VIS}, and Ch_{VIS-UV} are shown in Fig. 2, left. The spectrograms are composed of a series of laser-field–streaked XUV photoelectron spectra recorded as a function of delay between the XUV pulse and the subcycle field. A delay step of 0.2 fs was used, which safely allows sampling up to the highest frequency components (~0.9 PHz) in the waveform. Remarkably, each spectrogram reveals an isolated <200-as XUV pulse. This is a direct consequence of the substantial subcycle variation of field amplitude (Fig. 2, right), which provides an efficient temporal gate—via ionization confinement and/or energy filtering—for isolating a single attosecond burst in the XUV radiation emitted by the ionizing atoms. The feasibility of generating a robust isolated attosecond probe for a wide range of waveforms not only is required for the sampling of the transients but is most important also for the interrogation of processes triggered and/or controlled by the optical field transients.

Any of the retrieved electric field waveforms (Fig. 2, middle) permits full characterization of the properties of the apparatus and subsequently on-demand synthesis of prescribed fields. To this end, we used the waveform in Fig. 2A as a reference and retrieved the values of the control parameters of the system such as the field amplitudes, phase delays, and the CEPs of the three channels through the numerical band-pass filtering of the measured output waveform within the spectral ranges defined by Ch_{NIR}, Ch_{VIS}, and Ch_{VIS-UV}. The field transients shown in Fig. 2, B and C, were then synthesized by delaying Ch_{VIS-UV} in steps of $\pi/4$ (~200 as) with respect to the reference waveform. A more complex, nonsinusoidal transient, which is generated by delaying Ch_{NIR} so that the fields from the three channels cancel each other at the center of the waveform, is shown in Fig. 2D. The transient shown in Fig. 2E is generated via delay of Ch_{NIR} by ~π with respect to the waveform shown in Fig. 2D, resulting in a single intense field crest pointing in the opposite direction to the peak field in Fig. 2A. The full red and the dashed black lines in Fig. 2, middle, depict, respectively, waveforms measured or calculated from the constituent Ch_{NIR}, Ch_{VIS}, and Ch_{VIS-UV} fields retrieved from the reference waveform (Fig. 2A), with control parameters changed by known amounts with respect to those of the reference waveform. The agreement between prediction and measurement demonstrates controlled sub-femtosecond shaping, complete characterization, and reproducibility (synthesis) of petahertz field transients.

The instantaneous intensity shown in Fig. 2, right, reveals substantial variations of the strength of consecutive wave crests upon these transformations. The reference waveform (Fig. 2A) exhibits half cycles with relative intensities of (0.64, 1, 0.46) underpinning the subcycle character of the transient. Delaying Ch_{VIS-UV} gradually transforms the field into the highly asymmetric transient of Fig. 2C, with the temporal extension left almost unchanged. This transient carries its most intense field crest right at its leading edge, followed by half cycles of decreasing intensity (1, 0.89, 0.57), resulting in a sub-femtosecond rise time of its instantaneous intensity. On the other hand, a transient with its two most intense field crests separated by ~4.5 fs and a half-cycle virtually annihilated in between is revealed in Fig. 2D. The transient with the largest degree of temporal energy confinement is shown in Fig. 2F, with field crest intensities of (0.38, 1, 0.62) and with ~35% of its energy carried in a single wave crest.

Field ionization and its real-time sampling. We used transients with a central field crest ~1.7 times more intense than the adjacent half cycles (Fig. 3B) to ionize Kr atoms enclosed in a quasi-static gas cell (length $l \approx 0.74$ mm) at a density of $\approx 5.6 \times 10^{18}$ cm^{-3}. The gas cell was positioned at the laser focus, replacing the neon gas jet previously used for recording the streaking spectrograms shown in Fig. 3A (the experimental setup is shown in fig. S4). This procedure reveals the absolute timing of any process initiated or affected by the field transients with attosecond precision (SOM text, section 8).
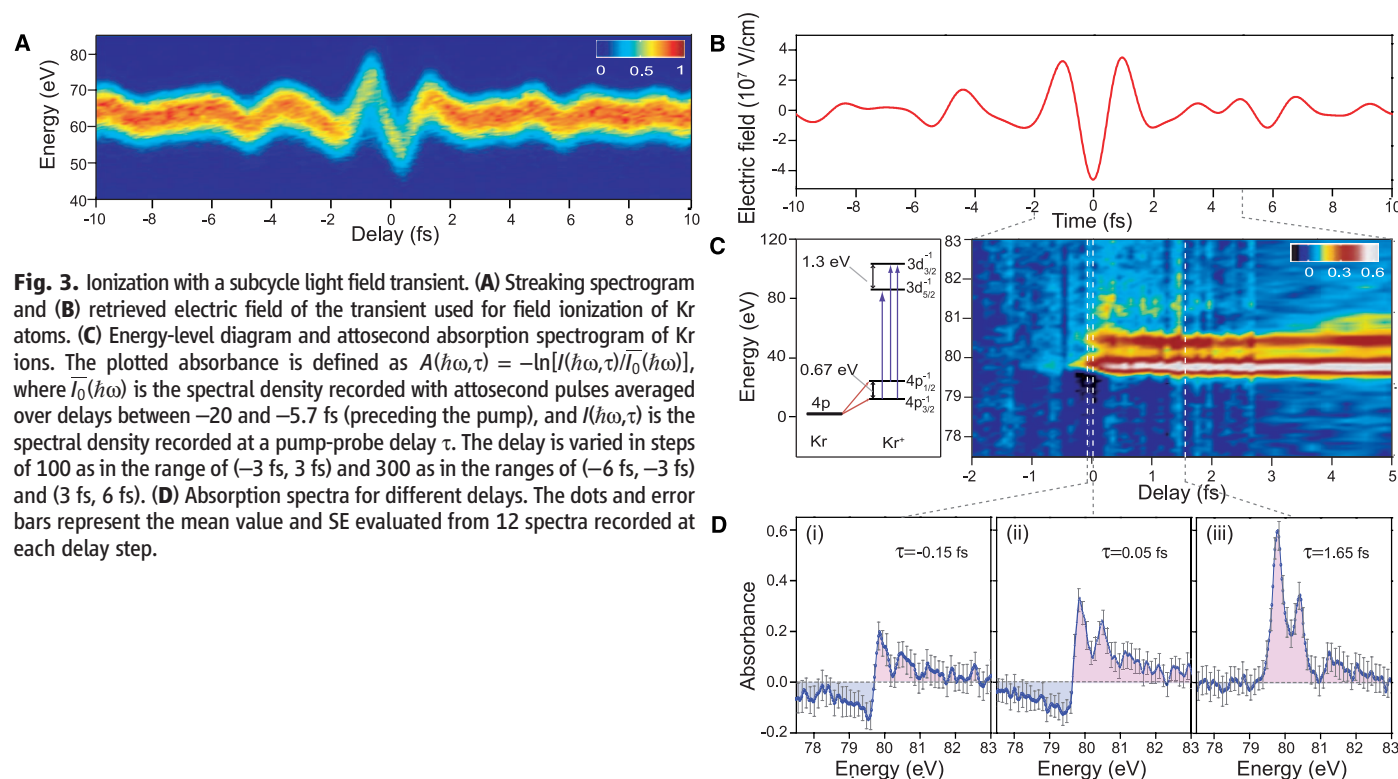
Fig. 3. Ionization with a subcycle light field transient. (**A**) Streaking spectrogram and (**B**) retrieved electric field of the transient used for field ionization of Kr atoms. (**C**) Energy-level diagram and attosecond absorption spectrogram of Kr ions. The plotted absorbance is defined as $A(\hbar\omega,\tau) = -\ln[I(\hbar\omega,\tau)/\overline{I_0}(\hbar\omega)]$, where $\overline{I_0}(\hbar\omega)$ is the spectral density recorded with attosecond pulses averaged over delays between −20 and −5.7 fs (preceding the pump), and $I(\hbar\omega,\tau)$ is the spectral density recorded at a pump-probe delay τ. The delay is varied in steps of 100 as in the range of (−3 fs, 3 fs) and 300 as in the ranges of (−6 fs, −3 fs) and (3 fs, 6 fs). (**D**) Absorption spectra for different delays. The dots and error bars represent the mean value and SE evaluated from 12 spectra recorded at each delay step.

We increased the intensity with an iris to $\approx 4.8 \times 10^{14}$ W/cm^2 and ionized ~16% of Kr atoms in the gas cell. We then probed strong-field ionization with a time-delayed attosecond pulse by measuring transient absorption spectra (*19*). Krypton ions created in their $4p^{-1}_{j=3/2}$ ground-state manifold and in the $4p^{-1}_{j=1/2}$ excited-state manifold, comprising four ($m_{j=3/2} = -3/2, -1/2, 1/2, 3/2$) and two ($m_{j=1/2} = -1/2, 1/2$) states, respectively, are promoted to the $3d^{-1}$ core-hole excited states by absorption of XUV photons from the attosecond pulse (Fig. 3C, left) (*36*). The resulting spectra transmitted through the gas cell were recorded as a function of the delay between the attosecond probe (pulse duration of ~200 as, centered at ~85 eV) and the ionizing field transient (pump), yielding the absorption spectrogram shown in Fig. 3C, right. The relevant transitions, $4p^{-1}_{3/2} \rightarrow 3d^{-1}_{5/2}$, $4p^{-1}_{1/2} \rightarrow 3d^{-1}_{3/2}$, and $4p^{-1}_{3/2} \rightarrow 3d^{-1}_{3/2}$, are indicated with arrows in the Fig. 3C level diagram. The absorption lines recorded at the leading edge of the ionizing field transient (Fig. 3D, i and ii, for example) have a characteristic profile revealing negative absorbance at photon energies below the resonances and positive absorbance above them (*37*). These transient line shapes gradually evolve to quasi-steady-state profiles toward the trailing edge of the ionizing field (Fig. 3D, iii).

State-selective sub-femtosecond tracing of field ionization. In order to relate the attosecond transient absorption spectra with ion population dynamics, we have performed numerical simulations by treating the generated Kr ions within a simplified, three-level model using the density matrix formalism (SOM text, section 3). The simulations reproduce well the experimental data (fig. S5) and demonstrate—in agreement with previous studies (*38*, *39*)—that the distortions of the transient absorption spectra are due to the synthesized pump field acting on the XUV-initiated, time-dependent ionic polarization response. Moreover, our simulations (based on an adiabatic tunnel-ionization calculation) suggest that—under the conditions of our experiments—the emerging absorption lines coincide with the population dynamics of the relevant ionic states, permitting retrieval of their transient evolution from the peak absorbances with good (~10%) accuracy (fig. S9). Figure 4A shows the sub-femtosecond evolution of the effective transient population in the ground state manifold $4p^{-1}_{j=3/2}$ (black dots), defined as $\rho^{eff}_{3/2,3/2}(t) = \rho^{(±1/2)}_{3/2,3/2}(t) + a\rho^{(±3/2)}_{3/2,3/2}(t)$, where $a = 2/3$ reflects the higher transition cross-section for the ($m_j = ±1/2$) transitions between $4p^{-1}_{j=3/2}$ and $3d^{-1}_{5/2}$ states; the $4p^{-1}_{j=1/2}$ manifold population $\rho^{(±1/2)}_{1/2,1/2}(t)$ is represented by black diamonds. These populations are retrieved from the $4p^{-1}_{3/2} \rightarrow 3d^{-1}_{5/2}$ and $4p^{-1}_{1/2} \rightarrow 3d^{-1}_{3/2}$ absorbances versus pump-probe delay, respectively. Because attosecond streaking is performed

in the same apparatus, this evolution can be directly timed and contrasted with the evolution of the ionizing field $[\,|E_L(t)|^2$, shown by the dashed line].

The buildup of the retrieved ionic populations exhibits steps that are in synchrony with the field crests of the transient. This becomes even more evident from the population rates obtained by taking the time-derivative of the ionic populations in Fig. 4A. The ionization rate, which is estimated as $\frac{d}{dt}\rho^{eff}_{3/2,3/2}(t)$ and shown in Fig. 4B (dots and red line), exhibits three main features at the crests of the ionizing field. The main ionization burst is responsible for approximately 80% of the ion population and has a full width at half maximum (FWHM) of <0.7 fs, indicating a sub-

femtosecond confinement of field ionization. It is this confinement to a single field crest that allows quantitative evaluation of the time-dependent rate of optical field ionization and state-selective population dynamics. For the populations depicted, we evaluate a peak production rate for $\rho^{eff}_{3/2,3/2}(t)$ of $\Gamma_{peak} = (0.12 ± 0.01)$ fs^{-1} and for $\rho^{(±1/2)}_{1/2,1/2}(t)$ of $\Gamma_{peak} = (0.059 ± 0.009)$ fs^{-1}, which is in excellent agreement with results obtained by numerically integrating the Schrödinger equation of a single-active electron model in three dimensions (SOM text, section 6), yielding $\Gamma_{peak}(\rho^{eff}_{3/2,3/2}) = 0.13$ fs^{-1} and $\Gamma_{peak}(\rho^{(±1/2)}_{1/2,1/2}) = 0.059$ fs^{-1}, which also well reproduces details of the temporal evolution
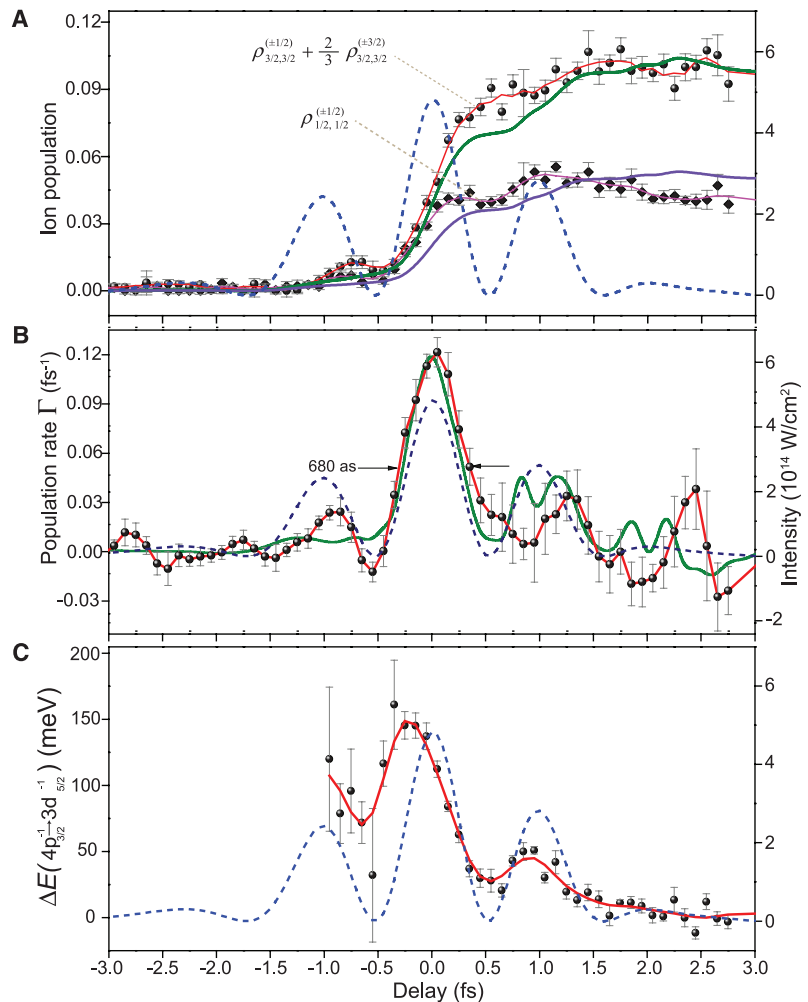
Fig. 4. Attosecond ionization and Stark effect dynamics in Kr$^+$. (**A**) Population dynamics in the ground-state $4p^{-1}_{j=3/2}$ manifold (dots), $\rho^{eff}_{3/2,3/2}(t)$, and in the excited-state $4p^{-1}_{j=1/2}$ manifold (diamonds), $\rho^{(±1/2)}_{1/2,1/2}(t)$, retrieved from the absorption spectrogram of Fig. 3C and contrasted with the instantaneous intensity (dashed line) as well as with the prediction of numerical simulations convolved with the XUV probe pulse duration (green and purple lines). (**B**) Ionization (population) rate $d\rho^{eff}_{3/2,3/2}(t)/dt$ evaluated from the data in (A) (dots and red line) in comparison with the theoretical prediction (green line). (**C**) Shift of the central energy of the $4p^{-1}_{3/2} \rightarrow 3d^{-1}_{5/2}$ transition evaluated by fitting a Lorentzian profile to the attosecond transient absorption spectra shown in Fig. 3C. Red curves in (A) to (C) and magenta curve in (A) are guides to the eye obtained by three adjacent point fast Fourier transform–smoothing.

of the ionic populations (Fig. 4A, green and purple lines, and B, green line).

Observation of the instantaneous optical Stark shift. The shift ΔE of quantum energy levels of atoms, molecules, or solids induced by an optical field $E_L(t)$—the ac Stark shift (40)—plays a central role in fundamental dynamical processes. So far, only cycle-averaged Stark effects have been accessible to experiments (41). If the laser frequency ω_L is much smaller than atomic resonance frequencies, the Stark shift of a nondegenerate atomic level is expected to instantly follow variations of the laser field: $\Delta E(t) = -1/2\mu E_L^2(t)$, where $\mu = \mu(\omega_L)$ is the atomic polarizability (42). When an XUV pulse creates a coherent superposition of two states with a difference in their respective polarizabilities $\Delta\mu(\omega_L)$, the induced polarization oscillations experience a phase shift, which is approximately given by

$$\Delta\varphi_{\mathrm{dipole}}(t) \approx -\frac{\Delta\mu}{2\hbar}\int_{t_0}^{t} E_L^2(t')dt' \qquad (1)$$

where t_0 denotes the moment of arrival of the attosecond XUV pulse (with $\tau_{\mathrm{XUV}} \ll 2\pi/\omega_L$). The instantaneous Stark shift detunes the energy at which the atom most efficiently absorbs photons from the XUV probe pulse—in our case, by the $3d \rightarrow 4p$ transition in Kr^+ ions—and mod-

ulates the frequency of the respective coherent dipole emission. Because the decay of the emission lasts several field cycles ($\tau = \tau_{3d} \sim 7.5$ fs), the Stark effect does not merely shift but also reshapes the transient absorption lines shown in Fig. 3D, i and ii. Thanks to the nearly instantaneous triggering of the polarization oscillations and their subsequent rapid decay, signatures of the instantaneous ac Stark shift come to light in our transient absorption spectra (Fig. 4C), which is in agreement with our simulations (figs. S8 and S9).

Valence wavepacket with well-defined quantum phase. Attosecond probing of few-cycle–driven field ionization of Kr atoms has revealed the emergence of a valence electron wavepacket in the $4p$ subshell of the Kr^+ ensemble—as a consequence of liberation of electrons from the $4p_{j=3/2}$ as well as the $4p_{j=1/2}$ manifolds—separated in energy by spin-orbit coupling in the Kr atoms (19). By repeating this attosecond absorption spectroscopic experiment with our subcycle transient shown in Fig. 3B, and supplementing it with attosecond streaking, we can now launch a valence wavepacket within a sub-femtosecond interval and with sub-femtosecond absolute timing accuracy.

From the recorded absorption spectrogram (Fig. 5A), we retrieve (SOM text, section 4) the fractional populations of the six ionic states, in

the form of the diagonal matrix elements $\rho_{j,j'=j}^{(m_j)}$ of the reduced density matrix—$\rho_{3/2,3/2}^{(3/2)} + \rho_{3/2,3/2}^{(-3/2)} = 0.315 \pm 0.024$, $\rho_{3/2,3/2}^{(1/2)} + \rho_{3/2,3/2}^{(-1/2)} = 0.400 \pm 0.024$, $\rho_{1/2,1/2}^{(1/2)} + \rho_{1/2,1/2}^{(-1/2)} = 0.285 \pm 0.004$—and a degree of coherence of $g = 0.85 \pm 0.06$, which exceeds that measured in the previous experiment (19) by ~1.4 times and is unparalleled for long-lived (>1 fs) coherences in the valence shell. Our simulations [based on a state-of-the-art three-dimensional time-dependent configuration-interaction singles approach (43) that includes correlation dynamics between the field-generated hole and the photoelectron and has been extended to include spin-orbit interaction (44)] well predict the measured coherence as well as fractional populations in the $4p_{j=1/2}^{-1}$ and $4p_{j=3/2}^{-1}$ manifolds (SOM text, section 7).

The nearly perfect coherence is, once again, a direct consequence of the sub-femtosecond width of the ionization gate. This confinement, along with sub-femtosecond absolute timing information from streaking, has far-reaching consequences. The former allows launching of the wavepacket with a well-defined initial phase, whereas the latter permits reliable determination of this initial quantum phase. The retrieved phase $\phi(t)$ [equation 2 in (19)] of the quantum superposition is shown in Fig. 5, B and C, along with representative snapshots of the generated ensemble-averaged hole density distributions, as evaluated from our data in Fig. 5A. Linear extrapolation of $\phi(t)$ to "time zero," the birth of the hole at the peak of the ionizing field transient (Fig. 5B, blue line), yields $\phi(t_0) = (0.99 \pm 0.04)\pi$, which is in very good agreement with the prediction of our configuration-interaction–based simulations: $\phi(t_0) = 1.06\pi$. This initial quantum phase implies an elongated initial hole-density distribution aligned with the ionizing field vector, which is commensurate with our intuitive expectation.

Outlook. Subcycle engineering of optical field transients opens new prospects for steering the atomic-scale motion of electrons (15) with the electric force of light and for driving complex valence-shell dynamics in molecules (45). As a simple manifestation of enhanced control over valence shell dynamics, they allow sub-femtosecond temporal confinement of ionization and precise associated triggering of a wealth of subsequent electronic phenomena. They also provide an isolated attosecond photon probe for interrogating the unfolding electronic and—in molecules—nuclear motions by means of attosecond absorption and/or photoelectron spectroscopy, as well as an isolated electron probe for tracing these dynamics via electron diffraction (46) or high-harmonic interferometry (47). This constitutes a substantial extension of the repertoire of attosecond science, which was previously restricted to either triggering or probing electronic processes within a sub-femtosecond time window. The feasibility
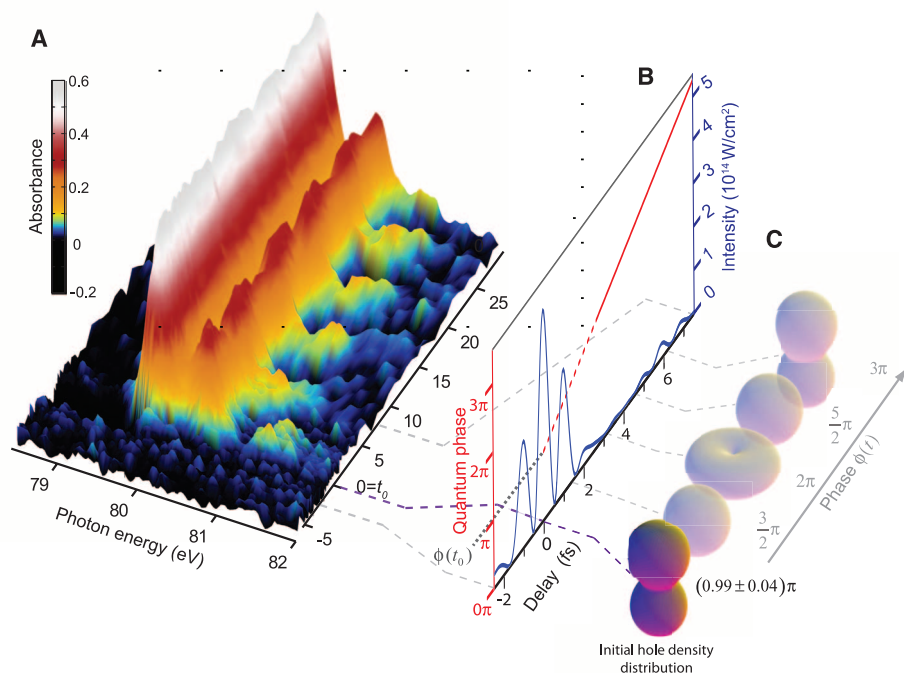
Fig. 5. Initial quantum phase and density distribution of a valence electron wavepacket. (**A**) Attosecond XUV transient absorption spectrogram of Kr atoms field-ionized by a subcycle field transient shown by the blue line in (**B**). Linear extrapolation of the retrieved quantum phase $\phi(t)$ [shown by the red line in (B)] to time zero as determined through attosecond streaking, allows access to the initial quantum phase $\phi(t_0) = (0.99 \pm 0.04)\pi$ of the valence electron wavepacket. (**C**) Ensemble-averaged initial hole density distribution in the valence shell at the instant of ionization and its subsequent evolution, as evaluated from (**A**).

of sub-femtosecond pump-probe interrogation of strong-field phenomena opens exciting research prospects. Real-time insight into multiple ionization in multi- to single-cycle laser fields, or into strong-field–induced electron correlations in atoms, molecules, or solids (*48*, *49*), are but a few examples.

References and Notes

1. J. F. Whitaker *et al.*, *Microelectron. Eng.* **12**, 369 (1990).
2. L. Xu *et al.*, *Opt. Lett.* **21**, 2008 (1996).
3. T. Brabec, F. Krausz, *Rev. Mod. Phys.* **72**, 545 (2000).
4. J. Reichert *et al.*, *Opt. Commun.* **172**, 59 (1999).
5. D. J. Jones *et al.*, *Science* **288**, 635 (2000).
6. S. A. Diddams *et al.*, *Phys. Rev. Lett.* **84**, 5102 (2000).
7. A. Apolonski *et al.*, *Phys. Rev. Lett.* **85**, 740 (2000).
8. T. Udem, R. Holzwarth, T. W. Hänsch, *Nature* **416**, 233 (2002).
9. S. T. Cundiff, J. Ye, *Rev. Mod. Phys.* **75**, 325 (2003).
10. A. Baltuška *et al.*, *Nature* **421**, 611 (2003).
11. M. Hentschel *et al.*, *Nature* **414**, 509 (2001).
12. R. Kienberger *et al.*, *Nature* **427**, 817 (2004).
13. G. Sansone *et al.*, *Science* **314**, 443 (2006).
14. E. Goulielmakis *et al.*, *Science* **320**, 1614 (2008).
15. M. F. Kling *et al.*, *Science* **312**, 246 (2006).
16. G. Sansone *et al.*, *Nature* **465**, 763 (2010).
17. M. Schultze *et al.*, *Science* **328**, 1658 (2010).
18. J. Mauritsson *et al.*, *Phys. Rev. Lett.* **105**, 053001 (2010).
19. E. Goulielmakis *et al.*, *Nature* **466**, 739 (2010).
20. S. Zherebtsov *et al.*, *Nat. Phys.*, published online 24 April 2011 (10.1038/nphys1983).
21. P. Eckle *et al.*, *Science* **322**, 1525 (2008).
22. S. E. Harris, A. V. Sokolov, *Phys. Rev. Lett.* **81**, 2894 (1998).
23. A. V. Sokolov, D. R. Walker, D. D. Yavuz, G. Y. Yin, S. E. Harris, *Phys. Rev. Lett.* **85**, 562 (2000).
24. J. Q. Liang, M. Katsuragawa, F. L. Kien, K. Hakuta, *Phys. Rev. Lett.* **85**, 2474 (2000).
25. A. V. Sokolov, D. R. Walker, D. D. Yavuz, G. Y. Yin, S. E. Harris, *Phys. Rev. Lett.* **87**, 033402 (2001).
26. T. Suzuki, M. Hirai, M. Katsuragawa, *Phys. Rev. Lett.* **101**, 243602 (2008).
27. Z.-M. Hsieh *et al.*, *Phys. Rev. Lett.* **102**, 213902 (2009).
28. H.-S. Chan *et al.*, *Science* **331**, 1165 (2011).
29. R. K. Shelton *et al.*, *Science* **293**, 1286 (2001).
30. M. Yamashita, K. Yamane, R. Morita, *IEEE J. Sel. Top. Quantum Electron.* **12**, 213 (2006).
31. S. Rausch, T. Binhammer, A. Harth, F. X. Kärtner, U. Morgner, *Opt. Express* **16**, 17410 (2008).
32. G. Krauss *et al.*, *Nat. Photonics* **4**, 33 (2010).
33. K. Okamura, T. Kobayashi, *Opt. Lett.* **36**, 226 (2011).
34. E. Goulielmakis *et al.*, *Science* **317**, 769 (2007).
35. E. Goulielmakis *et al.*, *Science* **305**, 1267 (2004).
36. This indicates that relative to the ground state configuration, a hole (or electron vacancy) is created in the nl_j^{-1} nl subshell, where j denotes the total angular momentum and m_j its projection on the z axis, the latter being aligned with the laser polarization.
37. B. R. Mollow, *Phys. Rev. A* **5**, 1522 (1972).
38. T. Unold, K. Mueller, C. Lienau, T. Elsaesser, A. D. Wieck, *Phys. Rev. Lett.* **92**, 157401 (2004).
39. C. H. B. Cruz, J. P. Gordon, P. C. Becker, R. L. Fork, C. V. Shank, *Int. J. Quant. Elec.* **24**, 261 (1988).
40. S. H. Autler, C. H. Townes, *Phys. Rev.* **100**, 703 (1955).
41. B. J. Sussman, *Am. J. Phys.* **79**, 477 (2011).
42. N. B. Delone, V. P. Krainov, *Phys. Uspekhi* **169**, 753 (1999).
43. L. Greenman *et al.*, *Phys. Rev. A* **82**, 023406 (2010).
44. S. Pabst, L. Greenman, P. J. Ho, D. A. Mazziotti, R. Santra, *Phys. Rev. Lett.* **106**, 053003 (2011).
45. F. Remacle, M. Nest, R. D. Levine, *Phys. Rev. Lett.* **99**, 183902 (2007).
46. M. Meckel *et al.*, *Science* **320**, 1478 (2008).
47. O. Smirnova *et al.*, *Nature* **460**, 972 (2009).
48. M. Gertsvolf, M. Spanner, D. M. Rayner, P. B. Corkum, *J. Phys. B* **43**, 131002 (2010).
49. M. Durach, A. Rusina, M. F. Kling, M. I. Stockman, *Phys. Rev. Lett.* **105**, 086803 (2010).

REPORTS

Observation of Correlated Particle-Hole Pairs and String Order in Low-Dimensional Mott Insulators

M. Endres,[1]* M. Cheneau,[1] T. Fukuhara,[1] C. Weitenberg,[1] P. Schauß,[1] C. Gross,[1] L. Mazza,[1] M. C. Bañuls,[1] L. Pollet,[2] I. Bloch,[1,3] S. Kuhr[1,4]

Quantum phases of matter are characterized by the underlying correlations of the many-body system. Although this is typically captured by a local order parameter, it has been shown that a broad class of many-body systems possesses a hidden nonlocal order. In the case of bosonic Mott insulators, the ground state properties are governed by quantum fluctuations in the form of correlated particle-hole pairs that lead to the emergence of a nonlocal string order in one dimension. By using high-resolution imaging of low-dimensional quantum gases in an optical lattice, we directly detect these pairs with single-site and single-particle sensitivity and observe string order in the one-dimensional case.

The realization of strongly correlated quantum many-body systems using ultracold atoms has enabled the direct observation and control of fundamental quantum effects (*1–3*). A prominent example is the transition from a superfluid (SF) to a Mott insulator (MI), occurring when interactions between bosonic particles on a lattice dominate over their kinetic energy (*4–8*). At zero temperature and in the limit where the ratio of kinetic energy over interaction energy vanishes, particle fluctuations are completely suppressed and the lattice sites are occupied by an integer number of particles. However, at a finite tunnel coupling but still in the Mott insulating regime, quantum fluctuations create correlated particle-hole pairs on top of this fixed-density background, which can be understood as virtual excitations. These particle-hole pairs fundamentally determine the properties of the MI, such as its residual phase coherence (*9*), and lie at the heart of superexchange-mediated spin interactions that form the basis of quantum magnetism in multicomponent quantum gas mixtures (*10–12*).

In a one-dimensional system, the appearance of correlated particle-hole pairs at the transition point from a SF to a MI is intimately connected to the emergence of a hidden string-order parameter $\mathcal{O}_P$ (*13*, *14*):

$$\mathcal{O}_P^2 = \lim_{l \to \infty} \mathcal{O}_P^2(l) = \lim_{l \to \infty} \left\langle \prod_{k \le j \le k+l} e^{i\pi \delta \hat{n}_j} \right\rangle \quad (1)$$

Here, $\delta \hat{n}_j = \hat{n}_j - \overline{n}$ denotes the deviation in occupation of the jth lattice site from the average background density, and k is an arbitrary position along the chain. In the simplest case of a MI with unity filling ($\overline{n} = 1$), relevant to our experiments, each factor in the product of operators in Eq. 1 yields -1 instead of $+1$ when a single-particle fluctuation from the unit back-

[1]Max-Planck-Institut für Quantenoptik, 85748 Garching, Germany. [2]Theoretische Physik, Eidgenössische Technische Hochschule (ETH) Zurich, 8093 Zurich, Switzerland. [3]Ludwig-Maximilians-Universität, 80799 Munich, Germany. [4]University of Strathclyde, Scottish Universities Physics Alliance, Glasgow G4 0NG, UK.

*To whom correspondence should be addressed. E-mail: manuel.endres@mpq.mpg.de